

# Comparison of photoacoustic imaging and histopathological examination in determining the dimensions of 52 human melanomas and nevi *ex vivo*

JENNY HULT,<sup>1</sup>  ABOMA MERDASA,<sup>1</sup>  AGNES PEKAR-LUKACS,<sup>2</sup> MAGNE TORDENGREN STRIDH,<sup>1</sup> AZIN KHODAVERDI,<sup>3</sup> JOHN ALBINSSON,<sup>1</sup>  BODIL GESSLEIN,<sup>1</sup> ULF DAHLSTRAND,<sup>1</sup>  LINN ENGQVIST,<sup>1</sup> YOUSEF HAMID,<sup>1</sup> DOUGLAS LARSSON ALBÈR,<sup>1</sup> BERTIL PERSSON,<sup>4</sup> TOBIAS ERLÖV,<sup>3</sup> RAFI SHEIKH,<sup>1</sup>  MAGNUS CINTHIO,<sup>3</sup>  AND MALIN MALMSJÖ<sup>1,\*</sup>

<sup>1</sup>Department of Clinical Sciences Lund, Ophthalmology, Lund University and Skåne University Hospital, Lund, Sweden

<sup>2</sup>Department of Pathology, Skåne University Hospital, Lund, Sweden

<sup>3</sup>Department of Biomedical Engineering, Faculty of Engineering, Lund University, Sweden

<sup>4</sup>Department of Dermatology, Skåne University Hospital, Lund, Sweden

\*[malin.malmsjo@med.lu.se](mailto:malin.malmsjo@med.lu.se)

**Abstract:** Surgical excision followed by histopathological examination is the gold standard for the diagnosis and staging of melanoma. Reoperations and unnecessary removal of healthy tissue could be reduced if non-invasive imaging techniques were available for presurgical tumor delineation. However, no technique has gained widespread clinical use to date due to shallow imaging depth or the absence of functional imaging capability. Photoacoustic (PA) imaging is a novel technology that combines the strengths of optical and ultrasound imaging to reveal the molecular composition of tissue at high resolution. Encouraging results have been obtained from previous animal and human studies on melanoma, but there is still a lack of clinical data. This is the largest study of its kind to date, including 52 melanomas and nevi. 3D multiwavelength PA scanning was performed *ex vivo*, using 59 excitation wavelengths from 680 nm to 970 nm. Spectral unmixing over this broad wavelength range, accounting for the absorption of several tissue chromophores, provided excellent contrast between healthy tissue and tumor. Combining the results of spectral analysis with spatially resolved information provided a map of the tumor borders in greater detail than previously reported. The tumor dimensions determined with PA imaging were strongly correlated with those determined by histopathological examination for both melanomas and nevi.

© 2021 Optical Society of America under the terms of the [OSA Open Access Publishing Agreement](#)

## 1. Introduction

Cutaneous melanoma is the most lethal form of skin cancer, and accounts for about 55,500 deaths worldwide per year [1]. Early-stage melanoma is highly curable, whereas the management of metastatic melanoma is challenging. Although newer therapies have improved the prognosis, the survival rates for metastatic melanoma are still poor [2]. Therefore, early and accurate diagnosis is essential for good treatment and patient survival [3].

The current gold standard for the diagnosis and treatment of melanoma is excisional biopsy and histopathological examination [4] in which the histomorphological, topographical and immunohistochemical features are assessed [5]. In cases of large lesions or lesions located in cosmetically sensitive areas, such as the face, ears, hands, feet and anogenital region, partial

biopsies are sometimes performed. Several problems are associated with diagnostic biopsies, including inaccurate histopathological tumor border determination, staging, and misdiagnosis, resulting in inadequate treatment [6–8].

The diagnostic excision of a skin lesion suspected of being melanoma, is generally performed with a 2 mm margin. If the lesion is confirmed to be a melanoma, a second, wide local excision is performed around the site, with a margin width depending on the histopathologically determined tumor thickness. European guidelines recommend a wide local excision with a 1-cm margin for melanomas  $\leq 2.0$  mm thick, while a 2-cm margin is recommended for thicker melanomas [9]. A sentinel lymph node biopsy is recommended for primary melanomas thicker than 1.0 mm [10].

A non-invasive technique capable of determining the dimensions of the melanoma could guide the diagnostic excision and thereby reduce the need for reoperation and unnecessary removal of healthy tissue. Several non-invasive methods have been developed for *in vivo* assessment of skin tumors. Apart from traditional dermoscopy, other examples are reflectance confocal microscopy, optical coherence tomography, multiphoton imaging, and high-frequency ultrasound. However, these methods are either limited by their imaging depth, or lack functional and molecular imaging capabilities [11,12]. Furthermore, the resolution in primary skin tumor imaging using magnetic resonance imaging and positron emission tomography is low.

Photoacoustic (PA) imaging is one of the most promising techniques in skin imaging, as it provides high-resolution 3D images down to a depth of several centimeters [13,14]. Using a combination of laser light and ultrasound, it takes advantage of the fact that sound scatters two to three orders of magnitude less than light, which enables optical contrast imaging at far greater depths than purely optical techniques [15]. In PA imaging, energy from non-ionizing laser pulses is absorbed by endogenous chromophores (such as melanin, oxygenated and deoxygenated hemoglobin (HbO<sub>2</sub> and HbR), collagen, and water) causing thermoelastic expansion that generates ultrasonic waves. The ultrasonic waves are then detected and translated into an image. PA imaging has been used successfully in animal studies to image melanomas in the skin [16–19], and in 2015, Zhou et al. demonstrated a high accuracy for depths up to 8 mm, and volume in *ex vivo* measurements of melanomas in mice [19]. Human studies have included PA detection of metastatic melanoma in sentinel lymph nodes both *ex vivo* and *in vivo* [20–23], and the detection of circulating melanoma cells [24–26]. However, PA imaging has not yet been approved for clinical use due to a lack of clinical data. Only five studies have been performed to date describing the first attempts to image melanoma in human skin [27–31], and these studies were limited in sample size and spectral information.

In the present study, 3D multiwavelength PA imaging was performed *ex vivo* on 52 suspected melanomas from 50 patients. Histopathological examination confirmed that 25 of these were melanomas, whereas the remaining 27 were nevi. The tumors were delineated using spectral unmixing at 59 excitation wavelengths, from 680 nm to 970 nm, accounting for multiple tissue chromophores. The tumor thickness and width were compared to those determined by histopathological examination.

## 2. Methods

### 2.1. Ethics

The experimental protocol for this study was approved by the Ethics Committee at Lund University, Sweden. The research adhered to the tenets of the Declaration of Helsinki as amended in 2008. Prior to surgery, all the patients participating in the study were given verbal and written information about the study, and the voluntary nature of participation. All patients gave their informed written consent.

## 2.2. Patients and lesion characteristics

The patients were recruited from the Department of Dermatology at Skåne University Hospital in Lund, southern Sweden. The inclusion criteria were age  $\geq 18$  years and a suspected primary melanoma. 50 patients with 52 suspected melanomas were included. Histopathological examination revealed that 25 were malignant melanomas and 27 were nevi. A summary of the patient characteristics is given in Table 1.

**Table 1. Patient characteristics and histopathological tumor summary**

Patient characteristics		Melanomas n=25		Nevi n = 27	
Age, mean and range (y)		66, range 38-94		50, range 20-77	
		N	%	N	%
Sex	Female/Male	9/16	36/64	14/13	52/48
Fitzpatrick skin type	I/II/III-VI/NA	2/21/1/1	8/84/4/4	3/22/2/0	11/81/7/0
<b>Histopathological tumor summary</b>					
Type of melanoma	Lentigo maligna	2	8		
	Melanoma in situ	9	36		
	Superficial spreading melanoma	13	52		
	Nodular melanoma	0	0		
	Lentigo maligna melanoma	1	4		
Grade of dysplasia	No dysplasia			13	48
	Low-grade dysplasia <sup>a</sup>			9	33
	Severe dysplasia			4	15
	Special site nevus			1	4
Radical excision	Yes/No	24/1	96/4	27/0	100/0
Minimum margin (mm)	< 1.0	2	8	4	15
	1.0-2.0	8	32	9	33
	2.1-5.0	14	56	13	48
	> 5.0	1	4	1	4
Tumor thickness <sup>b</sup> (mm)	$\leq 1.0$	23	92	25	93
	1.1-2.0	1	4	2	7
	2.1-4.0	1	4	0	0
	> 4.0	0	0	0	0
Tumor width (mm)	$\leq 5.0$ mm	7	28	19	70
	> 5.0 mm	18	72	8	30

<sup>a</sup>In the group low-grade dysplasia, we included 2 nevi that were graded as moderately dysplastic by the pathologist, in accordance with the 4<sup>th</sup> edition of the WHO Classification of Skin Tumours, published in 2018 (32).

<sup>b</sup>For melanoma *in situ*, tumor thickness measurements were only made for comparison with PA, and hence none of *in situ* melanomas were invasive. Tumor thickness measurements of melanoma *in situ* represent the epidermal thickness and include any benign tumor components beneath the epidermis.

## 2.3. Photoacoustic imaging

The PA setup for *ex vivo* imaging of pigmented skin lesions is illustrated in Fig. 1. The suspected melanomas were excised under local anesthesia by surgeons at the Department of Dermatology in Lund and placed in an isotonic saline solution before being transported to the Department of Ophthalmology, Lund. Any hair was cut off from the samples before scanning. The samples

were then mounted in a  $100 \times 70 \times 50$  mm custom made Plexiglas container using 1-2 Prolene 6-0 sutures (Ethicon, Bridgewater, NJ, USA) on each end of the lesion. A layer of black ultrasound-attenuating material was placed in the bottom of the container.

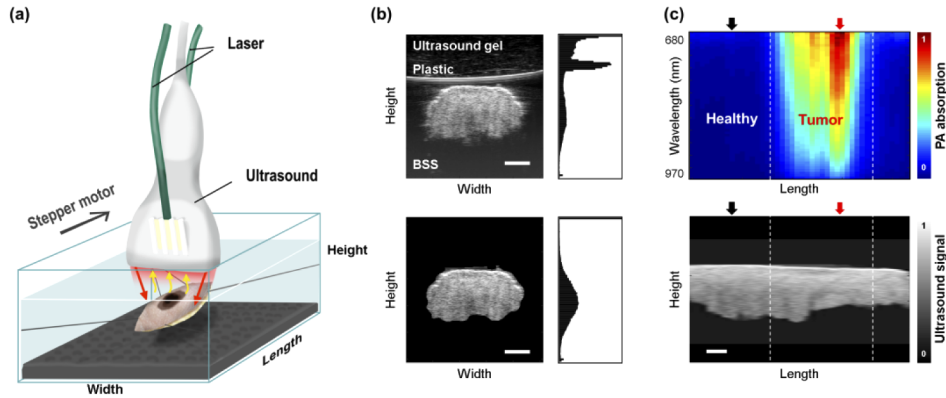


**Fig. 1.** Experimental setup and illustration of the pre-processing of the data for identification of the PA spectra from the tumor and healthy tissue. (a) The excised lesion was mounted in a Plexiglas container filled with isotonic saline using sutures and scanned using the PA imaging system. The PA probe consists of an ultrasound transducer with laser fiberoptic bundles attached. The lesion is irradiated with pulsed laser light (red arrows) causing thermoelastic expansion, which in turn generates acoustic waves (yellow arrows) that can be detected by an ultra-high-frequency ultrasound scanner. (b) The upper image shows the original brightness scan ultrasound image that includes the signal from the ultrasound gel, the protective plastic, and the isotonic saline. The lower image shows the signal after these unwanted components were removed. The insets to the right show the intensity histograms of the ultrasound images before and after pre-processing, where the sample and the background are clearly separated. (c) The upper image is a 2D heat map of the average PA absorption spectra for the entire sample, used to determine the preliminary PA spectra for the healthy tissue and tumor.

PA imaging was performed using a Vevo LAZR-X system (FUJIFILM VisualSonics Inc., Toronto, ON, Canada), which combines ultra-high-frequency ultrasound and photoacoustic linear-array-based multispectral imaging. During PA imaging, diagnostic ultrasound scans are interleaved with the laser pulses. In this system, an ultrasound transducer and a fiberoptic bundle are coupled to a 20 Hz tunable laser with a nanosecond pulse duration. The laser wavelength range used in this study was 680-970 nm. Two planar light beams, located either side of the ultrasound linear array, illuminate the skin surface.

To mimic a future *in vivo* setup, a 10 mm thick Aquaflex Ultrasound gel pad (Parker Laboratories Inc., Fairfield, CT, USA) with protective plastic was used to achieve an adequate distance between the laser fibers and the skin line. The photoacoustic waves were detected using one of two linear-array ultrasound transducers from VisualSonics Inc. The first, MX400, was used for lesions  $<13$  mm wide and has a central frequency of 30 MHz and bandwidth of 22-46 MHz, providing axial and lateral resolutions of  $50 \mu\text{m}$  and  $110 \mu\text{m}$ , respectively. The second, MX250, was used for lesions  $\geq 13$  mm wide and has a central frequency of 20 MHz and a bandwidth of 13-24 MHz, providing axial and lateral resolutions of  $75 \mu\text{m}$  and  $165 \mu\text{m}$ , respectively. The transducer was attached to a linear stepper motor (VisualSonics Inc.) to allow 2D multispectral images to be collected with 0.5 mm between each step. To prevent motion artifacts caused by the examiner, the transducer and stepper motor were attached to an adjustable arm (Mounting Accessory, GCX Corporation, Petaluma, CA, USA).

Prior to each measurement, the pulse fluence at each excitation wavelength was calibrated, and the signal at each wavelength was then corrected for the difference in photon flux with excitation

wavelength. Depending on the lesion size, 40-100 2D multispectral images were captured along each lesion. Each 2D image was captured at 59 excitation wavelengths from 680 to 970 nm, in steps of 5 nm. Hence, each pixel contained a single spectrum with 59 spectral components. The entire PA image was 512 pixels wide and 600-700 pixels high. The generation of each multispectral image took 15 seconds, and the duration of the whole 3D scan varied between 10 and 25 minutes, depending on the size of the sample. After PA imaging, the excised skin samples were placed in formaldehyde and sent for histopathological examination.

#### 2.4. Laser safety

Safety glasses providing protection in the wavelength range used (LSBGKG-33-BK, Phillips Safety Products, Middlesex, NJ, USA) were worn by all personnel. The laser radiant exposure and irradiance, as well as the acoustic mechanical index and intensity used have been described previously [33].

#### 2.5. Pre-processing of data

Raw data were exported from VisualSonics Vevo LAB 3.1.0 software and imported into MATLAB R2017b (MathWorks Inc., Natick, MA, USA) where all analysis was performed. Using the 3D multiwavelength scan, an approach was developed to identify the PA spectra from tumor and healthy tissue in each sample. Figure 1 provides an overview of the data analysis.

The first step involves pre-processing of the data using the ultrasound images to automatically remove unwanted signals from the ultrasound gel, protective plastic, and the saline solution. For this purpose, an intensity histogram (inset on the right of the images in Fig. 1(b)) is generated, using built-in MATLAB functions, from which a threshold can be set to distinguish the sample from the background. The Matlab function 'hist.m' was used to generate the histogram, but the number of bins was manually set to 100 to provide better resolution. The weighted average of the distribution was determined and set as the lower threshold. Any pixel intensity below this value was defined as belonging to the background. Two-dimensional median filtering was applied with the function 'medfilt2.m', using a bin size of  $30 \times 30$  pixels to ensure that smaller pixel regions within the sample that fell below the threshold value were included as signal, while small regions outside the sample that were recorded as a signal from the sample were defined as background.

In the second step, a spatially averaged PA spectrum is generated from each 2D image including all pixels extracted in the first step. Plotting all the PA spectra from each segment together in a heat map (Fig. 1(c)) shows how the absorption changes across the entire sample, where a clear increase can be seen in the region of the tumor. An ultrasound image showing the cross-section of the sample in the scan direction is shown below the spectral heat map, illustrating the structure of the sample from which the spectra were extracted. The segment exhibiting the highest PA absorption (indicated by the red arrows) is selected as the preliminary tumor spectrum, and a segment in which the PA absorption is low (indicated by the black arrows) is selected as the preliminary healthy tissue spectrum. These two spectra are then refined by localizing the region of interest in the respective 2D image, to extract an average spectrum from the top layer only. This refinement step reduces the undesired signal from healthy tissue in the spectrum representing the tumor. These two PA spectra were used consistently throughout the analysis, unless otherwise stated.

#### 2.6. Spectral unmixing and tumor mapping

Linear spectral unmixing was used to decompose the measured PA spectrum into a linear combination of so-called endmember spectra using the following equation:

$$M = \sum_{i=1}^N a_i S_i + w$$



where  $\mathbf{M}$  is a vector representing the measured PA spectrum,  $a_i$  the linear coefficients (or fractional abundances) of each endmember spectrum  $\mathbf{S}_i$ , and  $\mathbf{w}$  accounts for spectral noise. Ideally, only the number of endmember spectra ( $N$ ) that contribute to the measured spectrum should be included. However, when an endmember spectrum does not contribute, the factorization simply returns a value of 0 for the corresponding linear coefficient. Thus, including non-contributing endmember spectra is redundant, and does not reduce the accuracy of the overall fit.

In this study, spectral unmixing with two sets of endmember spectra was employed: one set representing known absorption spectra of the tissue chromophores  $\text{HbO}_2$ ,  $\text{HbR}$ , melanin, collagen and water (34), and the other including the two refined PA spectra representing healthy tissue and the tumor, as described above. One constraint placed on the spectral unmixing analysis is that the linear coefficients must be positive, which in practice means that negative absorption is not possible. This approach is used for the endmember set containing absorption spectra representing known chromophores to determine the relative contribution of each endmember.

An additional constraint was applied in the spectral unmixing analysis using only the refined PA spectra for tumor and healthy tissue, namely that the sum of the two linear coefficients must be 1. Consequently, a value of the linear coefficient representing the tumor endmember spectrum higher than 0.5 indicates that the measured PA spectrum better resembles the spectrum defined for the tumor, and a value of the linear coefficient representing the healthy endmember spectrum higher than 0.5 indicates that the the measured PA spectrum better resembles the spectrum defined for the healthy tissue. These criteria were then employed in a pixel-by-pixel analysis of each PA image to not only identify which pixels appear more like the tumor spectrum, but also to what extent. Each pixel identified as representing the tumor is color-coded and superimposed on the corresponding gray-scale ultrasound image. This approach was used for all the tumors analyzed and does not require manually setting an intensity threshold value, thereby making the analysis more objective. A comparison of this automatic threshold approach and manual intensity thresholding is shown in Fig. 5.

### 2.7. Multiwavelength 3D scanning

Multiwavelength 3D scanning was performed over the whole excised lesion, providing a map of the overall lesion architecture (a representative example is shown in Fig. 4). To obtain information on tumor cell distribution in the sample, spectral unmixing was performed on the multiwavelength recordings using the mean absorption spectra for melanoma and healthy tissue, as described above. The spectrally unmixed 2D images provided complete spatial information, that could be used to determine the greatest tumor width and thickness, which were compared to histopathological measurements.

### 2.8. Histopathological examination

The lesions were sectioned and stained with hematoxylin and eosin and thereafter scanned to provide digital images using Sectra IDS7 (Sectra AB, Linköping, Sweden). The dimensions of the lesion were determined by an experienced pathologist (A.P.). Since the histopathological sections were usually cut perpendicular to the longest side of the lesion, the PA measurements of tumor width were made along the same plane. In circular lesions, where the sectioning plane was difficult to identify, we used the greatest PA tumor width for comparison. The International Collaboration on Cancer Reporting [35] recommends that periadnexal extensions of melanoma (such as hair follicles and sweat glands) should not be included when measuring melanoma thickness. Therefore, the tumor thickness determined from the PA image was defined as the deepest part of the main tumor mass, whereas “tongues” of tumor extending more deeply were interpreted as periadnexal extensions and not used for correlation measurements. For thin melanomas within a thicker, benign tumor, we used the thickness of the whole tumor for comparison.

### 2.9. Statistical analysis

The PA signal strength varied from lesion to lesion. Therefore, the relative change in PA absorption was calculated for each lesion, by dividing the spectra for both tumor and healthy tissue by the mean spectrum acquired from healthy tissue, and the result is given in arbitrary units (a.u.). Data are expressed as mean values  $\pm$  SD, and the number of lesions is denoted N. Statistical analysis was performed using two-way ANOVA to compare the absorption spectra for the melanomas, nevi, and healthy tissue. Correlation analysis of the tumor width and thickness obtained from PA imaging and histopathological examination was performed using the Pearson correlation coefficient ( $r$ ). A value higher than 0.7 was considered indicative of a strong correlation, while a value between 0.5 and 0.7 was considered to indicate a moderate correlation.

## 3. Results

### 3.1. Spectral signatures of melanomas and nevi

PA imaging enabled non-invasive parallel acquisition of ultrasound and PA images, allowing anatomical co-localization of spectral and structural information. A significant difference was seen between the mean spectra from the melanomas and healthy tissue ( $p < 0.001$ ), as well as in the nevi, compared to the surrounding healthy tissue ( $p < 0.0001$ , Fig. 2). Furthermore, a significant difference was found between the mean spectra for melanomas and nevi ( $p = 0.0431$ ). However, the use of these spectra for differential diagnosis was not within the scope of this study, and would require subgroup analysis and a larger number of lesions.

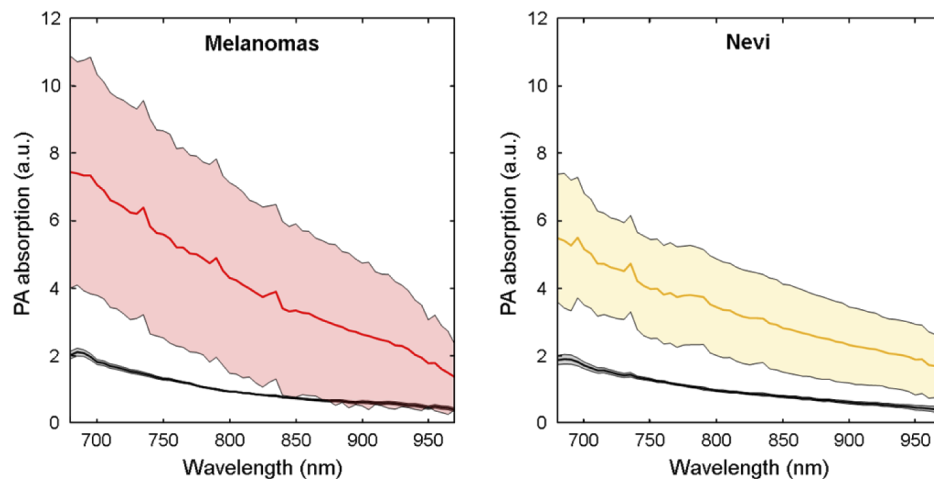


**Fig. 2.** PA absorption spectra obtained from (a) 25 melanomas (red line) and (b) 26 nevi (yellow line), compared to the surrounding healthy tissue (black line). Data are shown as mean  $\pm$  1 SD. Statistical analysis was performed using two-way ANOVA. Grubb's test was performed to identify outliers. One outlier was identified and removed from the nevi group. A clear difference can be seen between the spectral signatures from healthy tissue and melanomas ( $p < 0.001$ ) and between healthy tissue and nevi ( $p < 0.0001$ ).

### 3.2. Spectral unmixing and mapping

Spectral unmixing was used to determine the relative contributions of the five chromophore spectra: HbO<sub>2</sub>, HbR, melanin, collagen, and water (a representative example is shown in Fig. 3). The spectrum acquired from healthy tissue shows the presence of all endmembers, while the spectrum acquired from melanoma is dominated by melanin, with minor contributions from

HbO<sub>2</sub> and HbR. It is worth noting that there is a lack of collagen in the tumors, reflecting the presence of melanin-containing melanocytes in the lesions instead of an abundance of collagen. Spectral unmixing performed on the multiwavelength 3D scans provided a visual representation of the tumor borders in three dimensions in all lesions. A representative example of spectral unmixing on a melanoma *in situ* is shown in Fig. 4.

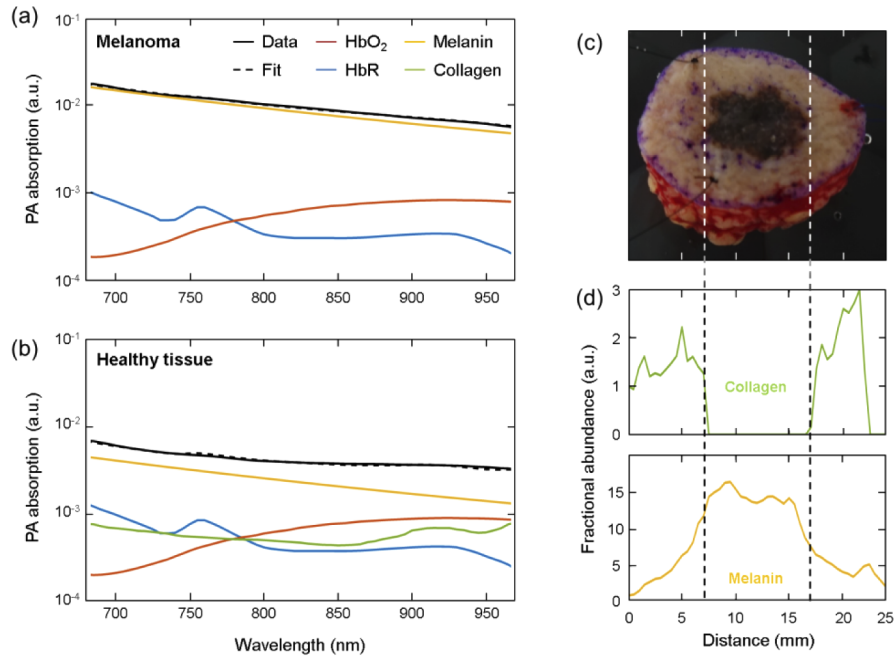


**Fig. 3.** Representative example of spectral unmixing of a lentigo maligna melanoma. Photoacoustic spectra (solid lines) from (a) a melanoma and (b) the surrounding healthy tissue, to which the linear spectral unmixing model was applied assuming the presence of endmember absorption spectra from melanin (yellow), HbO<sub>2</sub> (red), HbR (blue), and collagen (green) (water is not shown as the linear coefficient was zero). The fits including all endmembers are shown as dashed lines. (c) shows a photograph of a melanoma, and (d) graphs of the fractional abundance of collagen and melanin as a function of distance, analyzed using repeated 2D PA images from the multiwavelength 3D scan. Each fractional abundance is normalized to its initial value at distance = 0 mm to demonstrate the relative increase across the sample. It can be seen that there is an abundance of melanin and a lack of collagen in the melanoma.

### 3.3. Tumor thickness measurements

Results from the threshold approach described in the methods section were compared to those obtained when using single-wavelength PA imaging with manual intensity thresholding (Fig. 5), showing that the signal used to determine tumor borders varied greatly depending on the level of the threshold. A good measure of the tumor dimensions can be obtained by tuning the intensity threshold, although this procedure would be required for every sample examined, as the same intensity threshold would not be valid for all samples. The tumor thickness and width determined from PA imaging were compared to those determined by histopathological examination (Fig. 6, data given in supplementary material), showing a strong correlation for both melanoma and nevi. One lentigo maligna melanoma was excluded from the comparison of width because PA could



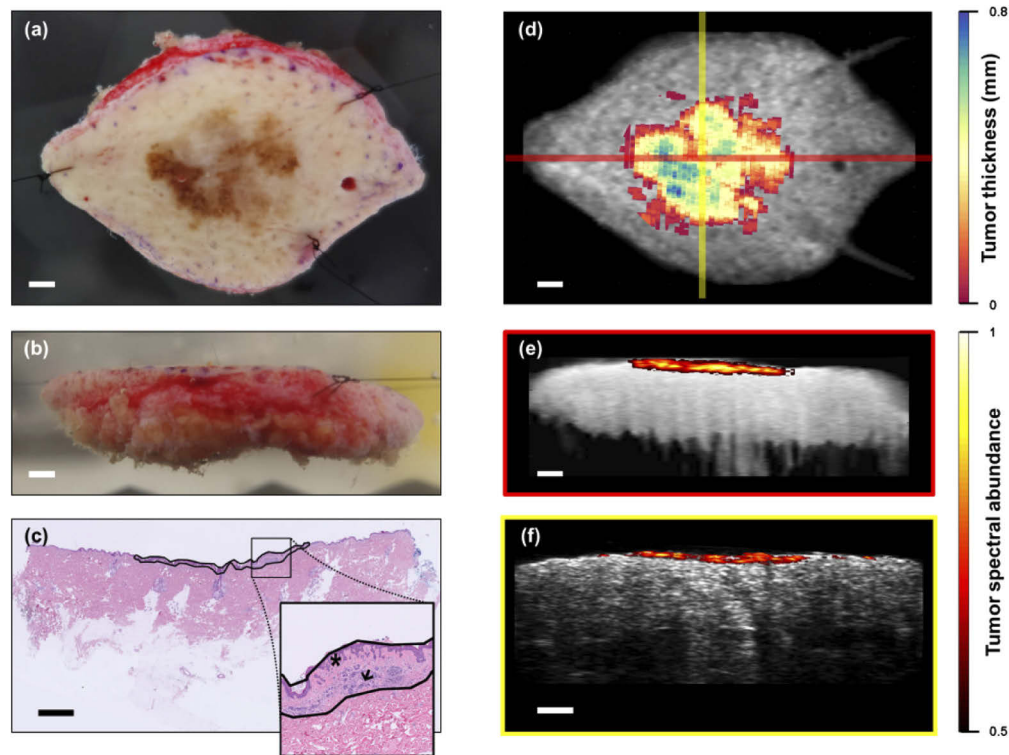


**Fig. 4.** Representative example of the results of the examination of a melanoma *in situ* with a benign dermal component. From above (a and d), longitudinal section (b and e), and transverse section (c and f). The left column (a-c) shows photographs and the histopathological image. The enlarged part of the histopathological image shows the melanoma *in situ* (star) and the benign dermal component (arrow). The small purple areas under the bordered region are hair follicles. Any malignant cells within the follicular epithelium are part of the *in situ* component and not included in measurements of tumor thickness. The right column (d-f) shows the images constructed after spectral unmixing was applied to the multiwavelength PA images. The information obtained from PA imaging is indicated by the colored pixels superimposed on the gray-scale ultrasound images. Spectral unmixing of the PA imaging enabled mapping of the lesion architecture and measurement of the greatest tumor width (11.1 mm) and thickness including the dermal component (0.6 mm), which were in good agreement with the values determined from the histopathological images (width 12.4 mm, and thickness 0.6 mm). Scale bars represent 2 mm.

not clearly distinguish between the signal from tumor and healthy tissue in the most superficial part of this lesion, and hence the PA width could not be measured.

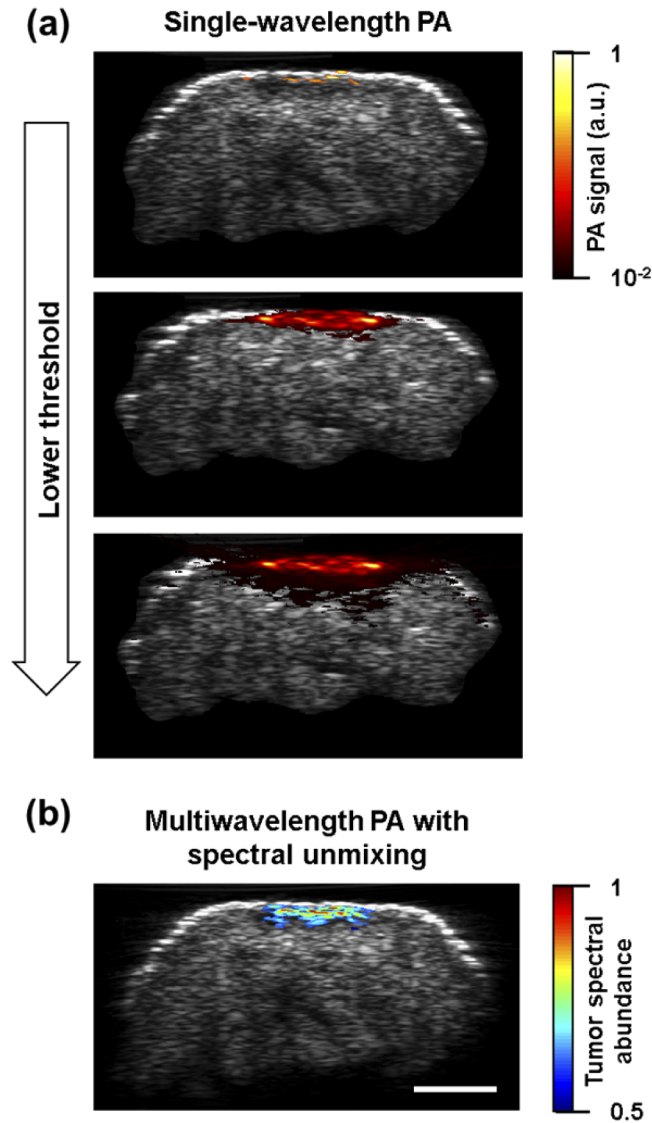


**Fig. 5.** (a) Illustration of manual intensity thresholding in a single-wavelength PA image (680 nm) where the threshold is successively lowered by 50%. The signal used to determine the tumor border depends greatly on the intensity threshold, leading to subjectivity on the part of the examiner. (b) The same sample analyzed by applying spectral unmixing to the multiwavelength PA image, where the threshold was set automatically. The latter technique was used to determine the tumor border in the present study.

For thin melanomas and nevi ( $\leq 1.0$  mm in thickness), PA overestimated the thickness slightly in 16 cases and underestimated the thickness slightly in 2 cases compared to histopathological measurements. For thick melanomas and nevi ( $> 1.0$  mm), PA underestimated the thickness slightly in 2 cases. For width measurements, PA overestimated the width in 24 cases and

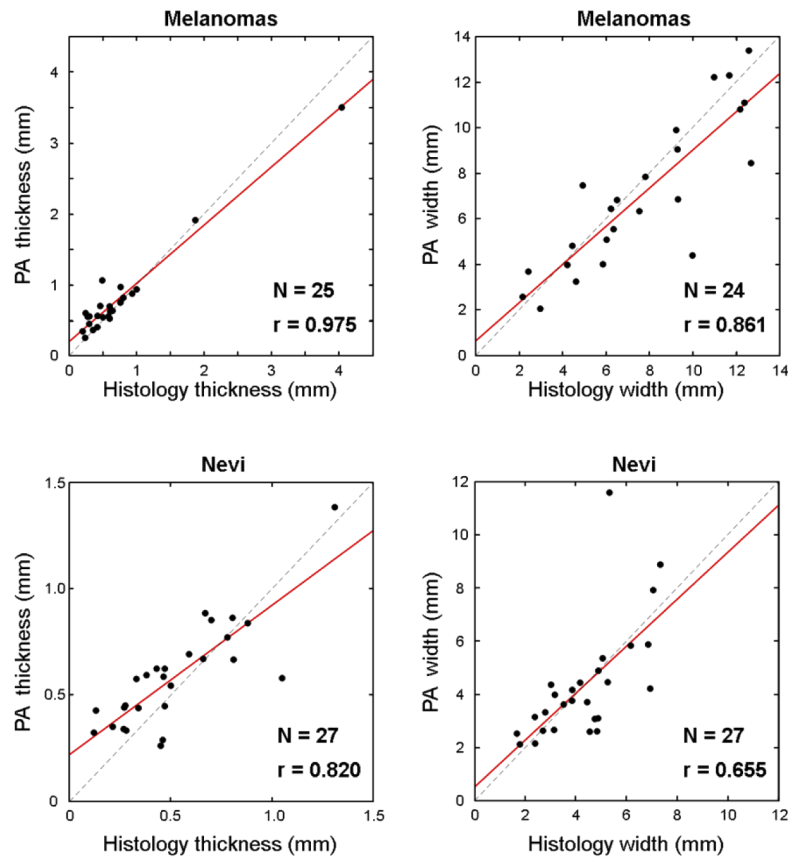


**Fig. 6.** Scatter plots showing the correlation between the tumor thickness and width measured using PA imaging and histopathological examination for the melanomas (above) and nevi (below). The Pearson correlation coefficients ( $r$ ) indicate a strong correlation for melanoma thickness and width, as well as the nevi thickness, and a moderate correlation for the nevi width.

underestimated the width in 23 cases. A difference of  $\pm 0.1$  mm or less was considered to indicate good agreement.

#### 4. Discussion

The results of the present study show the ability of PA imaging to map melanomas and nevi *ex vivo* non-invasively. To the best of the authors' knowledge, this is the most extensive study on both melanomas and nevi, in which detailed spectral analysis was performed. Spectral unmixing over a broad wavelength range in the 3D recordings enabled pixel-by-pixel analysis to provide complete spatial information on the tumor borders. The dimensions determined with PA imaging showed a strong correlation with those determined by histopathological examination for melanomas. In the case of nevi, the correlation was strong for thickness measurements and moderate for width measurements. Only a few studies have been published on the accuracy of tumor dimensions measured using PA imaging in humans [27–30], in which only a small number of lesions were studied.

Breathnach et al. measured the thickness of 23 benign pigmented lesions and 6 melanomas *in vivo* using PA imaging at 5 excitation wavelengths (680, 700, 750, 850, and 900 nm) for multiwavelength scans [29]. In a similar study, Park et al. measured the thickness of 5 melanomas with PA imaging *in vivo* also using 5 wavelengths (700, 756, 796, 866 and 900), while Kim et al. used 3 excitation wavelengths (680, 800 and 1064 nm) to measure one *in situ* human melanoma *ex vivo* [28,30]. Finally, Zhou et al. measured the thickness of 10 melanomas *ex vivo* using 1 wavelength (680 nm) [27]. Given the expected large variation in molecular composition between lesions, studies are required on larger numbers of patients to determine the clinical relevance of the results. Furthermore, only a few wavelengths have been used in previous studies, and the tumor border was defined based on high absorption amplitudes [27,29,30] or on the PA absorption signal of melanin alone [28,29], despite the opportunity for measurements based on the distribution of several different chromophores.

#### 4.1. The role of melanin and other chromophores

Melanin, produced by melanocytes in the epidermis, is an endogenous chromophore that absorbs light strongly in the range 600 to 1000 nm. If melanomas could be distinguished by their melanin content alone, single-wavelength PA imaging would suffice to provide contrast between the tumor and healthy tissue. However, keratinocytes and normal melanocytes, as well as macrophages, also contain melanin, which could lead to an overestimation of tumor dimensions. Another problem is that amelanotic melanomas, which account for approximately 10% of all invasive melanomas [36], contain little or no melanin. Also, the melanin content can differ depending on the melanoma stage [37]. A study on radiotherapy of 84 patients with melanoma revealed a significant reduction in melanin content, as determined by histopathological examination, in pT3 and pT4 melanomas, compared to pT1 and pT2 [37]. Furthermore, melanomas exhibit highly variable histological phenotypes [38], and a measurement technique that can identify minor deviations in molecular composition between tumor and healthy tissue is thus required to ensure accurate determination of tumor borders.

We assume that the fractions of HbO<sub>2</sub> and HbR are lower in our samples than they would have been if the same tissue had been examined *in vivo*, due to blood loss and vasoconstriction. Outside the cardiovascular system, HbR becomes oxygenated to HbO<sub>2</sub> by ambient oxygen [39]. HbO<sub>2</sub> will then auto-oxidize to methemoglobin due to the denaturation of recycling enzymes, and later to hemi- and hemochromes [40]. However, little is known about the transitions between different Hb derivatives *ex vivo* [39]. A forensic study on dry blood stains has shown that the fraction of HbO<sub>2</sub> decreases with time, but is still >60% of the initial dry state value for the first 24 hours [41], which could explain our finding of HbO<sub>2</sub> in the freshly excised sample (Fig. 3(a-b)).

A lentigo malignant melanoma was presented in Fig. 3 as an example of spectral unmixing. In general, we would expect a larger fraction of Hb in melanomas than in healthy tissue, but in this sample the Hb fraction was similar in the two. The reason for this is not known, but since capillaries are not uniformly distributed within a melanoma, the chosen region of interest could have contained less capillaries than other parts of the tumor. We did not choose other regions of interest for spectral unmixing of known chromophores to avoid user bias. Instead, we used the same approach for all samples when choosing the region of interest, as described in the methods section (pre-processing of data).

In the present study, 59 wavelengths were used over a broad spectral range (680-970 nm), which provided more detailed absorption spectra than in previous studies [28–30]. The use of more excitation wavelengths allows for a more robust analysis when determining the distribution of chromophores, as well as the identification of multiple chromophores with distinct spectral features. Unlike previous studies, we used several chromophore spectra representing different light-absorbing tissue components in our spectral analysis. Melanin is the strongest absorber in both melanoma and nevi, but to better determine the contribution of melanin to the PA signal it

is important to distinguish it from the absorption of HbO<sub>2</sub>, HbR, collagen, and water. In this study, we showed that collagen absorption was clearly reduced at the location of a melanoma, which improved the contrast between healthy tissue and tumor. To the best of our knowledge, no previous study has used collagen absorption in the spectral unmixing of skin tumors. In future delineation of tumors *in vivo*, we suggest that the absorption of HbO<sub>2</sub> and HbR should be included in the analysis, as this may reveal tumor specific vasculature which could affect the accuracy in determining the melanin concentration.

#### 4.2. Impact of intensity threshold

Breathnach et al. suggested that information obtained directly from a single-wavelength PA image could provide similar contrast between tumor and healthy tissue to that obtained when employing spectral unmixing [29]. Given that absorption across a broad spectral range should increase, single-wavelength PA imaging may suffice. However, we have demonstrated that this approach is too subjective, and ultimately depends on the intensity threshold set by the user to define whether the absorption signal is indicative of tumor or healthy cells. We have demonstrated that spectral unmixing of multiwavelength PA scans allows for a more unbiased determination of the intensity threshold used to distinguish between tumor and healthy tissue. This thresholding approach in analyzing PA images may even make the measurement of tumor dimensions more objective than histopathological analysis, in which fewer sections are analyzed and thicker or wider parts of the tumor might be missed.

#### 4.3. Scanning time

In this study, one multiwavelength scan took 10 to 25 minutes, depending on the sample size. The reason for this long scanning time was the number of wavelengths used, and the fact that we scanned the samples from edge to edge. The scanning time could be reduced by using fewer wavelengths and scanning a smaller distance along the sample. In the clinical setting, it may be more practical to identify the individual tumor spectrum, and then choose 5 wavelengths from this spectrum for the multiwavelength 3D scan. A multiwavelength scan would then take approximately 30 seconds per centimeter of sample scanned.

#### 4.4. Tumor dimensions

One limitation of this study was that most tumors (48 out of 52) were  $\leq 1.0$  mm thick. Determination of tumor thickness may be problematic using PA imaging as light is attenuated more with increasing tissue depth, and the attenuation depends on the tissue type [42]. Hence, the optical fluence (energy deposition) is not uniform within the tissue, which could further affect image reconstruction [43]. This phenomenon is called “spectral coloring” and occurs as incident photons successively penetrate deeper into tissue and experience wavelength-dependent absorption in different tissue layers [44]. Thus, PA spectra and measurements obtained from deeper tissue layers should be interpreted with caution.

Tzoumas et al. [45] presented a post-processing approach in which spectral coloring was taken into account and reduced the error in the estimation of oxygen saturation in human tissue by 17% at depths down to 1 cm. Bulsink et al. [46] presented similar findings using Monte Carlo simulations, although this method requires some prior knowledge of the tissue structure and its optical properties. In one of our recent studies on depth-resolved mapping of oxygenation during finger occlusion, blood in a digital artery between the dermis and hypodermis did not affect the PA signal from deeper tissue [47]. Hemoglobin is a strong light absorber, as is melanin (the major chromophore of interest in the present study), and although one could expect that the passage of light through these chromophores may lead to significant changes in the fluence spectrum deeper in the tissue, spectral coloring did not appear to be a significant factor in this previous study. The extent to which spectral coloring influences the detection of melanoma cannot be



deduced from the present study, although we hypothesize that it may be more difficult to measure the thickness of thicker tumors, as also suggested by Breathnach et al. [29]. In this study, for melanomas and nevi > 1.0 mm in thickness, PA was accurate in 3 tumors and underestimated the thickness slightly in 2 tumors.

While spectral coloring may lead to underestimation of the thickness of thicker tumors, shrinkage of surgically excised skin lesions may lead to an overestimation of PA measured tumor dimensions compared to histopathological measurements. It is well established that surgically excised skin samples shrink from the *in vivo* to the post-formalin fixation state [48–55]. Shrinkage occurs due to the retractile properties of skin [48,49] and possibly also due to formalin fixation [48,50]. The shrinkage of tumor tissue has not been established, although it has been suggested that tumor tissue may contract less than normal tissue because of a more inflexible structure [52]. In this study, PA overestimated the tumor thickness slightly for melanomas and nevi  $\leq 1$  mm thick. Our results are in line with those from a study by Dauendorffer et al., who reported that formalin caused a reduction in lesion thickness but not in lesion width [48]. Another possible explanation of the discrepancy could be that the PA measurements represent the true thickness, but that the histological sectioning might not have been performed exactly at the thickest part of the tumor.

#### 4.5. *Ex vivo versus in vivo, and the potential role of PA imaging in Mohs surgery*

In the current study, tumors were examined *ex vivo*, which eliminates motion artifacts and reduces the impact of chromophores in circulating blood. *Ex vivo* spectra are expected to differ from *in vivo* spectra regarding hemoglobin and water content, while other chromophores, such as melanin and collagen, are likely to be more constant. A PA imaging technique that enables multiwavelength 3D scanning *in vivo*, to generate images with high spatial resolution, was recently described by our group, where the importance of stabilization was emphasized [33]. To compensate for motion artefacts, the PA imaging data require post-processing, as recently described in a study on the human radial artery [56]. Spectral coloring should preferably also be corrected for using a post-processing technique [45,46]. Here, we have demonstrated two spectral unmixing approaches that yield either chromophore-specific contrast related to the tumor, or the classification of tissue as tumor or healthy tissue. After adaptation of the PA imaging scanning technique to *in vivo* conditions, the next step would involve a larger study on melanomas of different phenotypes and thicknesses *in vivo*.

In addition to developing a technique for future *in vivo* measurements, the *ex vivo* scanning of tumors could be useful for studies on the possible role of PA imaging in intraoperative micrographic control of surgical margins. Today, Mohs surgery is common practice for basal cell carcinoma and squamous cell carcinoma. This involves progressive removal and histopathological examination of thin layers of the tumor until only tumor-free tissue remains. Mohs surgery allows the removal of a skin cancer with a very narrow surgical margin and has a lower recurrence rate than standard excision for primary and recurrent basal cell carcinomas [57]. We recently presented a case of basal cell carcinoma on an eyelid, in which PA examination was used during surgery, possibly offering an alternative technique to histopathological examination for intraoperative micrographic control of the surgical margins [58]. PA imaging could be time-saving compared to histopathological examination of tissue during Mohs surgery, since freshly excised tissue can be scanned with high resolution in 3D without the need for freezing or sectioning. The use of Mohs surgery for melanoma is emerging but it is not widely used, probably due to concern that atypical melanocytes would not be detected in frozen sections [59]. However, in two large studies comparing Mohs surgery to wide local excision of melanomas, no difference was found in recurrence rates [59,60], and several other studies have shown that disease-specific survival following MMS for melanoma are comparable to or better than traditional excision [61–66]. Hence, there is clinical rationale for investigating the use of PA imaging for intraoperative micrographic control, not only for basal cell carcinomas, but also for melanomas.



#### 4.6. Limitations of current study

As mentioned previously, one limitation of this study was the small number of thick tumors. Another limitation was that most lesions were from patients with Fitzpatrick skin types I or II [48 out of 52], and only four lesions were from patients with Fitzpatrick skin type III or higher. It cannot be expected that the same difference in absorption spectra would have been seen in patients with a higher melanin content in healthy skin. Patients with Fitzpatrick skin types I and II have a higher risk of developing melanoma [67]. However, melanoma in patients with darker skin generally presents with greater tumor thickness, higher ulceration rates, increased rates of lymph-node-positive melanoma and a lower survival rate [68]. Future studies should include a wider range of skin types to investigate the effects of skin pigmentation on PA imaging.

#### 5. Conclusion

In conclusion, this study demonstrates the feasibility of PA imaging for non-invasive delineation of the borders of pigmented lesions *ex vivo*. It is the most comprehensive study to date, including 52 melanomas and nevi. A detailed 3D map of the tumor borders was obtained by applying linear spectral unmixing to the entire measured lesion in three dimensions on a pixel-by-pixel basis. Acquiring detailed spectral information over a broad spectral range (680–970 nm) allowed several tissue chromophores to be used in spectral analysis, providing greater contrast between tumor and healthy tissue, and thus more accurate determination of tumor borders. The dimensions determined with PA imaging were strongly correlated with those determined by histopathological examination for both melanomas and nevi. Techniques to correct for spectral coloring and movement artefacts need to be implemented, and thereafter a large clinical trial *in vivo* will be required before PA imaging can be considered as a clinical diagnostic tool. PA imaging has the potential to provide presurgical tumor dimensions to guide the complete surgical excision of primary melanomas.

**Funding.** Swedish Government Grant for Clinical Research; Skåne University Hospital (SUS) Research Grants; Skåne County Council Research Grants; Lund University Grant for Research Infrastructure; the Swedish Cancer Foundation; Crown Princess Margaret's Foundation (KMA); Friends of the Visually Impaired Association in the county of Gävleborg; Foundation for the Visually Impaired in the County of Malmöhus; Lund Laser Center Research Grant; IngaBritt and Arne Lundberg's Research Foundation; the Swedish Eye Foundation; the Cronqvist Foundation; the Swedish Medical Association.

**Acknowledgments.** We would like to thank the staff at the Department of Dermatology, Lund, for their valuable contributions.

**Disclosures.** The authors declare no conflicts of interest.

**Data availability.** Data underlying the results presented in this paper are not publicly available at this time but may be obtained from the authors upon reasonable request.

#### References

1. D. Schadendorf, A. C. J. van Akkooi, C. Berking, K. G. Griewank, R. Gutzmer, A. Hauschild, A. Stang, A. Roesch, and S. Ugurel, "Melanoma," *Lancet* **392**(10151), 971–984 (2018).
2. S. Ugurel, J. Rohmel, P. A. Ascierto, J. C. Becker, K. T. Flaherty, J. J. Grob, A. Hauschild, J. Larkin, E. Livingstone, G. V. Long, P. Lorigan, G. A. McArthur, A. Ribas, C. Robert, L. Zimmer, D. Schadendorf, and C. Garbe, "Survival of patients with advanced metastatic melanoma: the impact of MAP kinase pathway inhibition and immune checkpoint inhibition - Update 2019," *Eur. J. Cancer* **130**, 126–138 (2020).
3. M. Rastrelli, S. Tropea, C. R. Rossi, and M. Alaibac, "Melanoma: epidemiology, risk factors, pathogenesis, diagnosis and classification," *In Vivo* **28**(6), 1005–1011 (2014).
4. C. Garbe, T. Amaral, K. Peris, A. Hauschild, P. Arenberger, L. Bastholt, V. Bataille, V. Del Marmol, B. Dreno, M. C. Fargnoli, J. J. Grob, C. Holler, R. Kaufmann, A. Lallas, C. Lebbe, J. Malvehy, M. Middleton, D. Moreno-Ramirez, G. Pellacani, P. Saiag, A. J. Stratigos, R. Vieira, and I. Zalaudek, "Eggermont AMM, European Dermatology Forum tEaO-D-O, the European Organization for R. Treatment of C. European consensus-based interdisciplinary guideline for melanoma. Part 2: Treatment - Update 2019," *Eur. J. Cancer* **126**, 159–177 (2020).
5. A. N. Crowson, C. Magro, and M. C. Mihm Jr., "Unusual histologic and clinical variants of melanoma: implications for therapy," *Curr. Oncol. Rep.* **9**(5), 403–410 (2007).

6. J. C. Ng, S. Swain, J. P. Dowling, R. Wolfe, P. Simpson, and J. W. Kelly, "The impact of partial biopsy on histopathologic diagnosis of cutaneous melanoma: experience of an Australian tertiary referral service," *Arch. Dermatol.* **146**(3), 234–239 (2010).
7. V. H. Stell, H. J. Norton, K. S. Smith, J. C. Salo, and R. L. White Jr., "Method of biopsy and incidence of positive margins in primary melanoma," *Ann. Surg. Oncol.* **14**(2), 893–898 (2007).
8. D. J. Karimipour, J. L. Schwartz, T. S. Wang, C. K. Bichakjian, J. S. Orringer, A. L. King, C. C. Huang, and T. M. Johnson, "Microstaging accuracy after subtotal incisional biopsy of cutaneous melanoma," *J. Am. Acad. Dermatol.* **52**(5), 798–802 (2005).
9. C. G. Ethun and K. A. Delman, "The importance of surgical margins in melanoma," *J. Surg. Oncol.* **113**(3), 339–345 (2016).
10. S. L. Wong, M. B. Faries, E. B. Kennedy, S. S. Agarwala, T. J. Akhurst, C. Ariyan, C. M. Balch, B. S. Berman, A. Cochran, K. A. Delman, M. Gorman, J. M. Kirkwood, M. D. Moncrieff, J. S. Zager, and G. H. Lyman, "Sentinel lymph node biopsy and management of regional lymph nodes in melanoma: American Society of Clinical Oncology and Society of Surgical Oncology Clinical Practice Guideline Update," *J. Clin. Oncol.* **36**(4), 399–413 (2018).
11. J. Malvehy and P. G. Dermoscopy, "Confocal microscopy and other non-invasive tools for the diagnosis of non-melanoma skin cancers and other skin conditions," *Acta. Derm. Venereol.* **97**(218), 22–30 (2017).
12. L. Smith and S. Macneil, "State of the art in non-invasive imaging of cutaneous melanoma," *Skin Res. Technol.* **17**(3), 257–269 (2011).
13. C. Kim, T. N. Erpelding, L. Jankovic, M. D. Pashley, and L. V. Wang, "Deeply penetrating in vivo photoacoustic imaging using a clinical ultrasound array system," *Biomed. Opt. Express* **1**(1), 278–284 (2010).
14. L. Lin, P. Hu, J. Shi, C. M. Appleton, K. Maslov, L. Li, R. Zhang, and L. V. Wang, "Single-breath-hold photoacoustic computed tomography of the breast," *Nat. Commun.* **9**(1), 2352 (2018).
15. J. Yao and L. V. Wang, "Photoacoustic tomography: fundamentals, advances and prospects," *Contrast Media Mol. Imaging* **6**(5), 332–345 (2011).
16. J. T. Oh, M. L. Li, H. F. Zhang, K. Maslov, G. Stoica, and L. V. Wang, "Three-dimensional imaging of skin melanoma in vivo by dual-wavelength photoacoustic microscopy," *J. Biomed. Opt.* **11**(3), 034032 (2006).
17. Y. Wang, D. Xu, S. Yang, and D. Xing, "Toward in vivo biopsy of melanoma based on photoacoustic and ultrasound dual imaging with an integrated detector," *Biomed. Opt. Express* **7**(2), 279–286 (2016).
18. Y. Zhou, W. Xing, K. I. Maslov, L. A. Cornelius, and L. V. Wang, "Handheld photoacoustic microscopy to detect melanoma depth in vivo," *Opt. Lett.* **39**(16), 4731–4734 (2014).
19. Y. Zhou, G. Li, L. Zhu, C. Li, L. A. Cornelius, and L. V. Wang, "Handheld photoacoustic probe to detect both melanoma depth and volume at high speed in vivo," *J. Biophotonics* **8**(11-12), 961–967 (2015).
20. I. Stoffels, S. Morscher, I. Helfrich, U. Hillen, J. Leyh, N. C. Burton, T. C. Sardella, J. Claussen, T. D. Poeppel, H. S. Bachmann, A. Roesch, K. Griewank, D. Schadendorf, M. Gunzer, and J. Klode, "Metastatic status of sentinel lymph nodes in melanoma determined noninvasively with multispectral optoacoustic imaging," *Sci. Transl. Med.* **7**(317), 317ra199 (2015).
21. I. Stoffels, P. Jansen, M. Petri, L. Goerd, T. J. Brinker, K. G. Griewank, T. D. Poeppel, D. Schadendorf, and J. Klode, "Assessment of nonradioactive multispectral optoacoustic tomographic imaging with conventional lymphoscintigraphic imaging for sentinel lymph node biopsy in melanoma," *JAMA Netw. Open* **2**(8), e199020 (2019).
22. G. C. Langhout, D. J. Grootendorst, O. E. Nieweg, M. W. Wouters, J. A. van der Hage, J. Jose, H. van Boven, W. Steenbergen, S. Manohar, and T. J. Ruers, "Detection of melanoma metastases in resected human lymph nodes by noninvasive multispectral photoacoustic imaging," *Int. J. Biomed. Imaging* **2014**, 1–7 (2014).
23. D. J. Grootendorst, J. Jose, M. W. Wouters, H. van Boven, J. Van der Hage, T. G. Van Leeuwen, W. Steenbergen, S. Manohar, and T. J. Ruers, "First experiences of photoacoustic imaging for detection of melanoma metastases in resected human lymph nodes," *Lasers Surg. Med.* **44**(7), 541–549 (2012).
24. P. Hai, Y. Qu, Y. Li, L. Zhu, L. Shmuylovich, L. A. Cornelius, and L. V. Wang, "Label-free high-throughput photoacoustic tomography of suspected circulating melanoma tumor cells in patients in vivo," *J. Biomed. Opt.* **25**(03), 1–17 (2020).
25. R. M. Weight, P. S. Dale, and J. A. Viator, "Detection of circulating melanoma cells in human blood using photoacoustic flowmetry," *Annu. Int. Conf. IEEE Eng. Med. Biol. Soc.* **2009**, 106–109 (2009).
26. E. I. Galanzha, Y. A. Menyaev, A. C. Yadem, M. Sarimollaoglu, M. A. Juratli, D. A. Nedosekin, S. R. Foster, A. Jamshidi-Parsian, E. R. Siegel, I. Makhoul, L. F. Hutchins, J. Y. Suen, and V. P. Zharov, "In vivo liquid biopsy using cytophone platform for photoacoustic detection of circulating tumor cells in patients with melanoma," *Sci. Transl. Med.* **11**(496), eaat5857 (2019).
27. Y. Zhou, S. V. Tripathi, I. Rosman, J. Ma, P. Hai, G. P. Linette, M. L. Council, R. C. Fields, L. V. Wang, and L. A. Cornelius, "Noninvasive determination of melanoma depth using a handheld photoacoustic probe," *J. Invest. Dermatol.* **137**(6), 1370–1372 (2017).
28. B. Park, C. H. Bang, C. Lee, J. H. Han, W. Choi, J. Kim, G. S. Park, J. W. Rhie, J. H. Lee, and C. Kim, "3D wide-field multispectral photoacoustic imaging of human melanomas in vivo: a pilot study," *J. Eur. Acad. Dermatol. Venereol.* **35**, 669 (2020).

29. A. Breathnach, E. Concannon, J. J. Dorairaj, S. Shaharan, J. McGrath, J. Jose, J. L. Kelly, and M. J. Leahy, "Preoperative measurement of cutaneous melanoma and nevi thickness with photoacoustic imaging," *J. Med. Imag.* **5**(1), 1 (2018).
30. J. Kim, Y. H. Kim, B. Park, H. M. Seo, C. H. Bang, G. S. Park, Y. M. Park, J. W. Rhie, J. H. Lee, and C. Kim, "Multispectral ex vivo photoacoustic imaging of cutaneous melanoma for better selection of the excision margin," *Br. J. Dermatol.* **179**(3), 780–782 (2018).
31. N. Liu, Z. Chen, and D. Xing, "Integrated photoacoustic and hyperspectral dual-modality microscopy for co-imaging of melanoma and cutaneous squamous cell carcinoma in vivo," *J. Biophotonics* **13**(8), e202000105 (2020).
32. D. Elder, D. Massi, R. Scolyer, and R. Willemze, *WHO Classification of Tumours* 4th ed. (IARC, 2018).
33. R. Sheikh, M. Cinthio, U. Dahlstrand, T. Erlov, M. Naumovska, B. Hammar, S. Zackrisson, T. Jansson, N. Reistad, and M. Malmjö, "Clinical translation of a novel photoacoustic imaging system for examining the temporal artery," *IEEE Trans. Ultrason. Ferroelectr. Freq. Control.* **66**(3), 472–480 (2019).
34. S. L. Jacques, "Optical properties of biological tissues: a review," *Phys. Med. Biol.* **58**(11), R37–R61 (2013).
35. R. A. Scolyer, M. J. Judge, A. Evans, D. P. Frishberg, V. G. Prieto, J. F. Thompson, M. J. Trotter, M. Y. Walsh, N. M. Walsh, and D. W. Ellis, "International Collaboration on Cancer R. Data set for pathology reporting of cutaneous invasive melanoma: recommendations from the International Collaboration on Cancer Reporting (ICCR)," *Am. J. Surg. Pathol.* **37**(12), 1797–1814 (2013).
36. E. Wee, R. Wolfe, C. McLean, J. W. Kelly, and Y. Pan, "Clinically amelanotic or hypomelanotic melanoma: anatomic distribution, risk factors, and survival," *J. Am. Acad. Dermatol.* **79**(4), 645–651.e4 (2018).
37. A. A. Brozyna, W. Jozwicki, K. Roszkowski, J. Filipiak, and A. T. Slominski, "Melanin content in melanoma metastases affects the outcome of radiotherapy," *Oncotarget.* **7**(14), 17844–17853 (2016).
38. D. Massi, D. Mihic-Probst, D. Schadendorf, R. Dummer, and M. Mandala, "Dedifferentiated melanomas: morpho-phenotypic profile, genetic reprogramming and clinical implications," *Cancer Treat. Rev.* **88**, 102060 (2020).
39. G. Zadora and A. Menzyk, "In the pursuit of the Holy Grail of forensic science—spectroscopic studies on the estimation of time since deposition of bloodstains," *TrAC, Trends Anal. Chem.* **105**, 137–165 (2018).
40. J. Dissing, A. Sondervang, and S. Lund, "Exploring the limits for the survival of DNA in blood stains," *J. Forensic Leg. Med.* **17**(7), 392–396 (2010).
41. R. H. Bremmer, D. M. de Bruin, M. de Joode, W. J. Buma, T. G. van Leeuwen, and M. C. Aalders, "Biphasic oxidation of oxy-hemoglobin in bloodstains," *PLoS One* **6**(7), e21845 (2011).
42. S. Zackrisson, S. van de Ven, and S. S. Gambhir, "Light in and sound out: emerging translational strategies for photoacoustic imaging," *Cancer Res.* **74**(4), 979–1004 (2014).
43. M. N. Fadhel, E. Hysi, H. Assi, and M. C. Kolios, "Fluence-matching technique using photoacoustic radiofrequency spectra for improving estimates of oxygen saturation," *Photoacoustics* **19**, 100182 (2020).
44. B. Cox, J. G. Laufer, S. R. Arridge, and P. C. Beard, "Quantitative spectroscopic photoacoustic imaging: a review," *J. Biomed. Opt.* **17**(6), 061202 (2012).
45. S. Tzoumas, A. Nunes, I. Olefir, S. Stangl, P. Symvoulidis, S. Glasl, C. Bayer, G. Multhoff, and V. Ntziachristos, "Eigenspectra optoacoustic tomography achieves quantitative blood oxygenation imaging deep in tissues," *Nat. Commun.* **7**(1), 12121 (2016).
46. R. Bultink, M. Kuniyil Ajith Singh, M. Xavierselvan, S. Mallidi, W. Steenbergen, and K. J. Francis, "Oxygen saturation imaging using LED-based photoacoustic system," *Sensors* **21**(1), 283 (2021).
47. A. Merdasa, J. Bunke, M. Naumovska, J. Albinsson, T. Erlöv, M. Cinthio, N. Reistad, R. Sheikh, and M. Malmjö, "Photoacoustic imaging of the spatial distribution of oxygen saturation in an ischemia-reperfusion model in humans," *Biomed. Opt. Express* in press.
48. J. N. Dauendorffer, S. Bastuji-Garin, S. Guero, N. Brousse, and S. Fraitag, "Shrinkage of skin excision specimens: formalin fixation is not the culprit," *Br. J. Dermatol.* **160**(4), 810–814 (2009).
49. W. Salmhofer, E. Rieger, H. P. Soyer, J. Smolle, and H. Kerl, "Influence of skin tension and formalin fixation on sonographic measurement of tumor thickness," *J. Am. Acad. Dermatol.* **34**(1), 34–39 (1996).
50. N. Gregory, M. Mulvaney, T. Pattison, J. Hill, J. A. Carlson, and V. Goncharuk, "Shrinkage of skin excision specimens and downcoding," *Arch. Dermatol.* **139**(4), 542–543 (2003).
51. M. K. Silverman, F. M. Golomb, A. W. Kopf, C. M. Grin-Jorgensen, K. A. Vossaert, J. P. Doyle, and M. J. Levenstein, "Verification of a formula for determination of preexcision surgical margins from fixed-tissue melanoma specimens," *J. Am. Acad. Dermatol.* **27**(2), 214–219 (1992).
52. C. Blasdale, F. G. Charlton, S. C. Weatherhead, P. Ormond, and C. M. Lawrence, "Effect of tissue shrinkage on histological tumour-free margin after excision of basal cell carcinoma," *Br. J. Dermatol.* **162**(3), 607–610 (2010).
53. F. M. Golomb, J. P. Doyle, C. M. Grin, A. W. Kopf, M. K. Silverman, and M. J. Levenstein, "Determination of preexcision surgical margins of melanomas from fixed-tissue specimens," *Plast. Reconstr. Surg.* **88**(5), 804–809 (1991).
54. G. Blasco-Morente, C. Garrido-Colmenero, I. Perez-Lopez, S. Carretero-Garcia, A. Martin-Castro, S. Arias-Santiago, and J. Tercedor-Sanchez, "Study of shrinkage of cutaneous surgical specimens," *J. Cutaneous Pathol.* **42**(4), 253–257 (2015).
55. M. J. Kerns, M. A. Darst, T. G. Olsen, M. Fenster, P. Hall, and S. Grevey, "Shrinkage of cutaneous specimens: formalin or other factors involved?" *J. Cutaneous Pathol.* **35**(12), 1093–1096 (2008).

56. T Erlov, R Sheikh, U Dahlstrand, J Albinsson, M Malmstö, and M Cinthio. Regional motion correction for in vivo photoacoustic imaging in humans using interleaved ultrasound images. *Biomed. Opt. Express* 2021. In press.
57. E. van Loo, K. Mosterd, G. A. Krekels, M. H. Roozeboom, J. U. Ostertag, C. D. Dirksen, P. M. Steijlen, H. A. Neumann, P. J. Nelemans, and N. W. Kelleners-Smeets, "Surgical excision versus Mohs' micrographic surgery for basal cell carcinoma of the face: a randomised clinical trial with 10 year follow-up," *Eur. J. Cancer* **50**(17), 3011–3020 (2014).
58. U. Dahlstrand, R. Sheikh, and M. Malmstö, "Photoacoustic imaging for intraoperative micrographic control of the surgical margins of eyelid tumours," *Acta Ophthalmol.* **98**(2), e264–e265 (2020).
59. A. Nosrati, J. G. Berliner, S. Goel, J. McGuire, V. Morhenn, J. R. de Souza, Y. Yeniy, R. Singh, K. Lee, M. Nakamura, R. R. Wu, A. Griffin, B. Grimes, E. Linos, M. M. Chren, R. Grekin, and M. L. Wei, "Outcomes of melanoma in situ treated with mohs micrographic surgery compared with wide local excision," *JAMA Dermatol.* **153**(5), 436–441 (2017).
60. L. Chin-Lenn, T. Murynka, J. G. McKinnon, and J. P. Arlette, "Comparison of outcomes for malignant melanoma of the face treated using Mohs micrographic surgery and wide local excision," *Dermatol. Surg.* **39**(11), 1637–1645 (2013).
61. G. M. Bricca, D. G. Brodland, D. Ren, and J. A. Zitelli, "Cutaneous head and neck melanoma treated with Mohs micrographic surgery," *J. Am. Acad. Dermatol.* **52**(1), 92–100 (2005).
62. J. H. Kunishige, D. G. Brodland, and J. A. Zitelli, "Surgical margins for melanoma in situ," *J. Am. Acad. Dermatol.* **66**(3), 438–444 (2012).
63. J. R. Etzkorn, J. F. Sobanko, R. Elenitsas, J. G. Newman, H. Goldbach, T. M. Shin, and C. J. Miller, "Low recurrence rates for in situ and invasive melanomas using Mohs micrographic surgery with melanoma antigen recognized by T cells 1 (MART-1) immunostaining: tissue processing methodology to optimize pathologic staging and margin assessment," *J. Am. Acad. Dermatol.* **72**(5), 840–850 (2015).
64. S. Felton, R. S. Taylor, and D. Srivastava, "Excision margins for melanoma in situ on the head and neck," *Dermatol. Surg.* **42**(3), 327–334 (2016).
65. L. E. Stigall, D. G. Brodland, and J. A. Zitelli, "The use of Mohs micrographic surgery (MMS) for melanoma in situ (MIS) of the trunk and proximal extremities," *J. Am. Acad. Dermatol.* **75**(5), 1015–1021 (2016).
66. S. M. Valentin-Nogueras, D. G. Brodland, J. A. Zitelli, L. Gonzalez-Sepulveda, and C. M. Nazario, "Mohs micrographic surgery using MART-1 immunostain in the treatment of invasive melanoma and melanoma in situ," *Dermatol. Surg.* **42**(6), 733–744 (2016).
67. L. Titus-Ernstoff, A. E. Perry, S. K. Spencer, J. J. Gibson, B. F. Cole, and M. S. Ernstoff, "Pigmentary characteristics and moles in relation to melanoma risk," *Int. J. Cancer* **116**(1), 144–149 (2005).
68. H. M. Gloster Jr. and K. Neal, "Skin cancer in skin of color," *J. Am. Acad. Dermatol.* **55**(5), 741–760 (2006); quiz 61–4.